Clim Dyn (2015) 45:1617–1634
DOI 10.1007/s00382-014-2417-9

Interannual variability of the spring atmospheric heat source over the Tibetan Plateau forced by the North Atlantic SSTA

Yangfan Cui · Anmin Duan · Yimin Liu · Guoxiong Wu

Received: 14 October 2014 / Accepted: 13 November 2014 / Published online: 2 December 2014

Abstract Data analysis indicates that the interannual variability of the spring atmospheric heat source over the Tibetan Plateau (TP) depends largely on the intensity of the overlying subtropical westerly jet (WJ), which is closely related to the early spring (February–March–April) sea surface temperature anomaly (SSTA) tripole pattern over the North Atlantic, i.e., the SSTA tripole pattern with a warm core to the southeast of Newfoundland and two cold cores to the south of Iceland and southeast of Bermuda, respectively. Such an SSTA pattern can be regarded as a response to the atmospheric forcing of the preceding January–February–March North Atlantic Oscillation. Numerical experiment results from both linear baroclinic model with an idealized diabatic heating profile and an atmospheric general circulation model with prescribed SSTA forcing demonstrate that the warm core alone of the tripole pattern can stimulate a steady downstream Rossby wave train, which further intensifies the spring WJ over the TP. As a result, a positive anomaly of surface sensible heating occurs over most parts of the TP, whereas the precipitation and corresponding latent heating is characterized by a seesaw pattern with a positive/negative anomaly over the northern/southern TP. Meanwhile, the air column radiation cooling effect is enhanced to a certain degree over the plateau. Further analysis suggests that the early spring SSTA over the North Atlantic may exert a seasonal-lagged impact upon the East Asian summer monsoon by modulating the thermal forcing over the TP.

Keywords Tibetan Plateau · Atmospheric heat source · Westerly jet · North Atlantic Oscillation · SSTA tripole pattern

Y. Cui · A. Duan (✉) · Y. Liu · G. Wu
The State Key Laboratory of Numerical Modelling for Atmospheric Sciences and Geophysical Fluid Dynamics (LASG), Institute of Atmospheric Physics, Chinese Academy of Sciences, P. O. Box 9804, Beijing 100029, China
e-mail: amduan@lasg.iap.ac.cn

Y. Cui
University of Chinese Academy of Sciences, Beijing 100049, China

1 Introduction

The Tibetan Plateau (TP) is located in the subtropical central and eastern Eurasian continent, acting as a huge, elevated atmospheric heat source (AHS) in summer but a heat sink in winter (Flohn 1957; Yeh et al. 1957; Yeh and Gao 1979; Wu et al. 2012). With seasonal evolution, the air column over the TP changes from an atmospheric heat sink to a source in boreal spring (March–April–May), with the dominant contribution from surface sensible heating (SH) before the monsoon onset (e.g., Yeh and Gao 1979; Shen et al. 1986; Yanai and Li 1994; Zhao and Chen 2001). Moreover, the air pump driven by SH over the TP can regulate the Asian summer monsoon onset and intensity because the heating effect along the sloping surface converges the air in the lower layer from the surrounding areas with ascending air flows that penetrate the isentropic surfaces and compensate for the surface SH (Wu et al. 1997, 2007). Results based on both data analysis and numerical simulation have revealed that a strong spring SH over the TP facilitates an early onset of East Asian summer monsoon (EASM), as well as strong monsoon circulation to its east and a dry and hot climate in central Asia to its west (e.g., Murakami and Ding 1982; Wu et al. 2007; Duan et al. 2013).

In comparison to the many studies on the thermal forcing effect of the TP on regional and hemispheric circulation

and climate, the large-scale factors contributing to the variation of the AHS over the TP receives much less attention. The mean altitude of the TP is more than 4,000 m above sea level and the surface flow is controlled mainly by the subtropical Westerly Jet (WJ) throughout most of the year, except summer (June–July–August), and the in situ land–air temperature difference presents high magnitude but a small relative change compared with the surface wind speed (Yeh and Gao 1979; Liu et al. 2012). Thus, the spring SH over the TP is closely related to the variation of the WJ according to the bulk formula (Duan and Wu 2009; Liu et al. 2012).

As a dominant atmospheric mode in the mid and high latitudes, the North Atlantic Oscillation (NAO), or Artic Oscillation (AO) for a hemispheric perspective, can modulate the interannual and interdecadal variability of the WJ over central and East Asia (e.g., Marshall et al. 2001, Gong and Ho 2003; Yang et al. 2004; Li et al. 2005, 2008; Wu et al. 2009). However, most of these studies focused on the possible connection between the wintertime NAO (AO) and the WJ based on data diagnosis, whereas the nature of the mechanism underlying the influence of the NAO (AO) on the spring WJ, especially the local response of the AHS over the TP, remains an open issue.

The NAO, which is prevalent during boreal winter strongly affects the oceans through latent and sensible heat exchanges (Cayan 1992a, b). The local weather noise and surface heat flux associated with NAO (Fan and Schneider 2012) usually drive a sea surface temperature anomaly (SSTA) tripole pattern in the North Atlantic in winter, i.e., a warm SSTA core in the mid-latitudes and two cold SSTA cores to its northeast and southeast sides (Cayan 1992a, b; Deser and Timlin 1997; Czaja and Frankignoul 2002; Zhou et al. 2006). Such a SSTA tripole pattern, in turn, produces NAO-like atmospheric anomalies, indicating a positive feedback between the NAO and the SSTA tripole pattern (Watanabe and Kimoto 2000; Pan 2005). In this context, the present study aims to address how the early spring SSTA over the North Atlantic, as a result of the preceding NAO, affects the remote WJ above the TP by changing the large-scale circulation, and how the subsequent local response of the spring AHS over the TP takes place and subsequently affects the EASM.

The remainder of the paper is structured as follows. The data and models used in the study are introduced in the following section. Section 3 focuses on a diagnosis of the data concerning the relationships among the SSTA over the North Atlantic, the subtropical WJ over eastern Eurasia, and the AHS over the TP. This is followed in Sect. 4 by reporting results from numerical simulations conducted to address how the SSTA leading mode over the North Atlantic modulates the WJ over the TP. The seasonal-lagged impacts of the spring AHS over the TP on the EASM are investigated in Sect. 5. Further discussion and conclusions are presented in Sect. 6.

2 Data and models

2.1 Data

The data used in this study were from the following sources:

1. Regular surface meteorological observations at 73 stations over the TP provided by the China Meteorology Administration (CMA) for the period 1980–2008. Data were gathered four times daily (0000, 0600, 1200, and 1800 UTC). Variables included surface air temperature (T_a), ground surface temperature (T_s), and wind speed at 10 m above the surface (V). Daily cloud amount (0–10 tenth of sky cover) and daily accumulated precipitation (Pr) records from 756 stations in China covering the same period were also used. The CMA routinely applies quality control procedures to eliminate erroneous data and ensure homogeneity.
2. The daily mean wind speed, temperature, and geopotential height at standard pressure levels, together with cloud amount, precipitation, and heat fluxes at the land surface and top of the atmosphere (TOA), covering the same period (1980–2008) were obtained from the Modern-Era Retrospective Analysis for Research and Application (MERRA) dataset (Rienecker et al. 2011).

Different reanalysis datasets provide different characterizations of meteorological fields over China (Liu et al. 2012), and thus the Japanese 25-year Reanalysis (JRA-25; Onogi et al. 2007) conducted by the Japan Meteorological Agency (JMA), the National Centers for Environmental Prediction/National Center for Atmospheric Research (NCAR) Reanalysis 1 (NCEP/NCAR; Kalnay et al. 1996), the NCEP/Department of Energy (NCEP/DOE) Reanalysis 2 (Kanamitsu et al. 2002), and the European Centre for Medium-Range Weather Forecasts (ECMWF) Re-Analysis Interim (ERA-Interim; Dee et al. 2011) were analyzed simultaneously. The MERRA reanalysis is provided at a horizontal resolution of 1.25° × 1.25° with 42 standard pressure levels; the JRA-25 reanalysis is provided at the same horizontal resolution but with 23 standard pressure levels; the NCEP/NCAR and NCEP/DOE reanalyses are provided at a horizontal resolution of 2.5° × 2.5° with 17 standard pressure levels; and the ERA-Interim dataset is provided at a horizontal resolution of 1.25° × 1.25° with 37 standard pressure levels.

3. Monthly SST data during the same period from the Met Office Hadley Centre Sea Surface Temperature (HadISST) dataset (Rayner et al. 2003), provided at a resolution of 1° × 1° (http://www.metoffice.gov.uk/hadobs/hadisst/data/download.html).
4. The NAO index from the Climate Prediction Center (http://www.cpc.ncep.noaa.gov/products/precip/CWlink/pna/nao.shtml).

The AHS defined by the gaining or losing of heat in the air column can be expressed as

$$AHS = SH + LH + RC, \tag{1}$$

where SH represents the surface sensible heat flux, LH is the latent heat released to the atmosphere due to condensation, and RC is the net radiation flux of the air column.

The bulk aerodynamic method is often used to calculate SH:

$$SH = Cp \times \rho \times C_{DH} \times V \times (T_s - T_a), \tag{2}$$

where $C_p = 1{,}005$ J kg^{-1} K^{-1} is the specific heat of dry air at constant pressure; ρ is the air density that decreases exponentially with elevation; C_{DH} is the dimensionless drag coefficient for heat, which generally increases with land surface roughness; and V is the wind speed 10 m above the ground. This procedure has been widely used in TP-related studies (e.g., Yeh and Gao 1979; Chen et al. 1985; Li et al. 2001). We assumed $\rho = 0.8$ kg m^{-3} (Yeh and Gao 1979) and $C_{DH} = 4 \times 10^{-3}$ (Li and Yanai 1996) for the central-eastern TP, and $C_{DH} = 4.75 \times 10^{-3}$ for the western TP (Li et al. 2000). Following Duan et al. (2013), SH was calculated based on Eq. (2) by using local 4-time daily observations at all 73 stations over the TP.

LH can be estimated by precipitation using the formula

$$LH = \Pr \times Lw \times \rho, \tag{3}$$

where $L_w = 2.5 \times 10^6$ J kg^{-1} is the condensation heat coefficient and $\rho = 1.0 \times 10^3$ kg m^{-3} is the water density.

The expression for RC in Eq. (1) is

$$RC = R_\infty - R_0 = \left(S_\infty^\downarrow - S_\infty^\uparrow\right) - \left(S_0^\downarrow - S_0^\uparrow\right) - \left(F_0^\downarrow - F_0^\uparrow\right) - F_\infty, \tag{4}$$

where R_∞ and R_0 are the net radiation values at the TOA and land surface respectively. S and F denote the shortwave and longwave radiation fluxes, and their subscripts "∞" and "0" denote the TOA and the ground surface, while the superscripts "$\downarrow$" and "$\uparrow$" represent downward and upward transport, respectively.

The linear trends of the data used in this study were all removed to help highlight the interannual variability.

2.2 Models

The linear baroclinic model (LBM) was a time-dependent model based on the primitive equations exactly linearized about a basic state (see Watanabe et al. 1999; Watanabe and Kimoto 2000; Watanabe and Jin 2003 for the mathematical expressions). The model variables, consisting of vorticity (ζ), divergence (D), temperature (T), and the logarithm of surface pressure (π), were horizontally represented by spherical harmonics having the resolution of T42 while being vertically discretized using a finite difference to 20 σ levels, in which five layers resided below $\sigma = 0.8$. The model also included three dissipation terms: a biharmonic horizontal diffusion with a damping timescale of 1 day for the smallest wave; very weak vertical diffusion (damping timescale of 1,000 days) to remove vertical noise arising from the finite difference; and Newtonian damping and Rayleigh friction as represented by a linear drag, which had a timescale of 1 day applied only to the lower boundary layers ($\sigma \geq 0.9$) and the uppermost two levels ($\sigma \leq 0.03$). With the dissipation terms adopted, the model response took about 20 days to approach a steady state. Therefore, the average of the last 5 days in the 30-day integration is analyzed in this paper.

The atmospheric general circulation model (AGCM) used in this study was SAMIL 2.4.7, which is the current version of the Spectral Atmospheric Model developed by the State Key Laboratory of Numerical Modeling for Atmospheric Sciences and Geophysical Fluid Dynamics, Institute of Atmospheric Physics (LASG/IAP). This model uses a horizontal resolution of R42 (2.81° longitude × 1.66° latitude) with 26 σ-p hybrid vertical layers that extend from the surface up to 2.19 hPa. The model dynamical framework employs a standard atmosphere subtraction scheme (Wu et al. 1996) to accurately calculate pressure gradient forces. The effects of gravity wave drag are included (Palmer et al. 1986). Convective precipitation is calculated according to the mass flux cumulus parameterization developed by Tiedtke (1989) with a modified closure assumption and organized entrainment and detrainment (Nordeng 1994; Song 2005). The cloud scheme is diagnostic, and is parameterized according to low-layer static stability and relative humidity (Slingo 1980, 1989). A statistical stratocumulus cloud scheme is also employed (Dai et al. 2004).

The model includes a non-local scheme that calculates the profile of eddy diffusivity, the scale of turbulent velocity, and the effects of non-local transport of heat and moisture (Holtslag and Boville 1993). The Sun–Edwards–Slingo (SES2) radiation scheme is used to model radiative transfer (Edwards and Slingo 1996; Sun 2005). In particular, monthly SST and sea ice are prescribed according to the 20-year climatology used by phase two of the Atmospheric

Model Intercomparison Project (AMIP II) (see http://www-pcmdi.llnl.gov/projects/amip/AMIP2EXPDSN/BCS_OBS/amip2_bcs.htm for details). These monthly-mean conditions are linearly interpolated to each integration step. This AGCM can successfully reproduce the climate-mean and seasonal evolution of circulation and precipitation in EASM regions (Wang et al. 2012a) and is being used to investigate the mechanical and thermal forcing of the TP on the Asian summer monsoon (Wu et al. 2012 ; Duan et al. 2013) and formation and variation of the AHS over the TP in winter (Yu et al. 2011a, b).

3 Influence of the spring SSTA tripole pattern over the North Atlantic on the WJ and AHS over the TP

3.1 500 hPa zonal wind over the TP and the North Atlantic SSTA

Figure 1a shows the first leading mode of empirical orthogonal function (EOF1) analysis for spring (March–April–May, MAM) 500 hPa zonal wind speed over and around the TP in MERRA reanalysis data, which is featured by a spatially uniform westerly with one center just located above the TP (36.2 % explained variance). The corresponding principle component (U_PC1) can well represent the (25°N–40°N, 60°E–120°E) domain-averaged zonal wind speed index (U_domain), with the correlation coefficient of

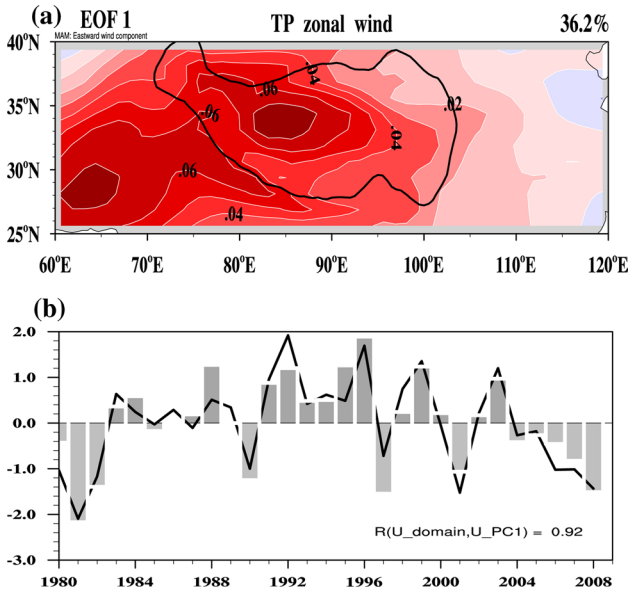

Fig. 1 **a** Spatial pattern of the first EOF mode (EOF1) for March–April–May (MAM) mean zonal wind speed at 500 hPa over and around the TP (25°–40°N, 60°–120°E) in MERRA reanalysis data during 1980–2008; **b** Normalized expansion coefficient of the EOF1 (U_PC1, *line*) and the normalized time series of domain-averaged (25°–40°N, 60°–120°E) zonal wind speed (U_domain, *bar*)

Table 1 Correlation coefficients between the domain-averaged 500 hPa zonal wind speed over the TP (25°–40°N, 60°–120°E) from five reanalysis datasets and the 73-station-averaged surface sensible heating (SH), latent heating (LH) released to the atmosphere due to condensation, and 10 m wind speed (*V*) over the TP area during spring (March–April–May) from 1980 to 2008

	ERA-Interim	MERRA	NCEP_NCAR	NCEP_DOE	JRA-25
SH	0.58**	0.59**	0.58**	0.57**	0.61**
LH	−0.18	−0.22	−0.12	−0.14	−0.22
V	0.51*	0.43*	0.49*	0.51*	0.50*

*, ** Statistical significance above the 95 and 99 % confidence levels, respectively

0.92, exceeding the 99.9 % confidence level (Fig. 1b). To demonstrate the relationship between the spring subtropical WJ and the AHS over the TP, we chose the domain-averaged 500 hPa zonal wind speed as the MAM WJ index in the following parts.

Table 1 shows the correlation coefficients between the spring WJ index calculated from five reanalysis datasets and the 73-station-averaged SH, LH, 10 m wind speed (*V*) over the TP. It is evident that both SH and *V* are significantly correlated with the WJ index, exceeding 95 % confidence level. However, the correlations between the WJ index and LH over the TP is not significant, suggesting that, in terms of the TP domain average, the connection between the WJ index and SH is closer than that with LH. This result agrees with Duan and Wu (2009), who found that the variation of spring SH over the TP is controlled primarily by the WJ. Considering the consistency in zonal wind speed among all five reanalysis datasets and the highest resolution, we chose the MERRA reanalysis in the following diagnosis.

The linkage between the spring WJ over the TP and the remote North Atlantic SST can be indicated by the lead-lag correlation patterns as shown in Fig. 2, in which one can see a clear SSTA tripole pattern, i.e., the SSTA tripole pattern with a warm core to the southeast of Newfoundland and two cold cores to the south of Iceland and southeast of Bermuda, respectively. The SSTA tripole pattern associated with the WJ index reaches its peak in February–March–April (FMA) and sustained throughout the whole spring and then decayed quickly during summer, suggesting it might lead the spring WJ over TP about 1 month.

Singular value decomposition (SVD) analysis is a method that can effectively isolate the coupled modes of variability between two fields (Bretherton et al. 1992). To reveal the connection between the WJ over the TP with North Atlantic SST more clearly, we performed SVD analysis on the MAM zonal wind speed at 500 hPa over the TP and the FMA SST field over the North Atlantic. Figure 3a, b display the leading SVD modes (SVD1) of

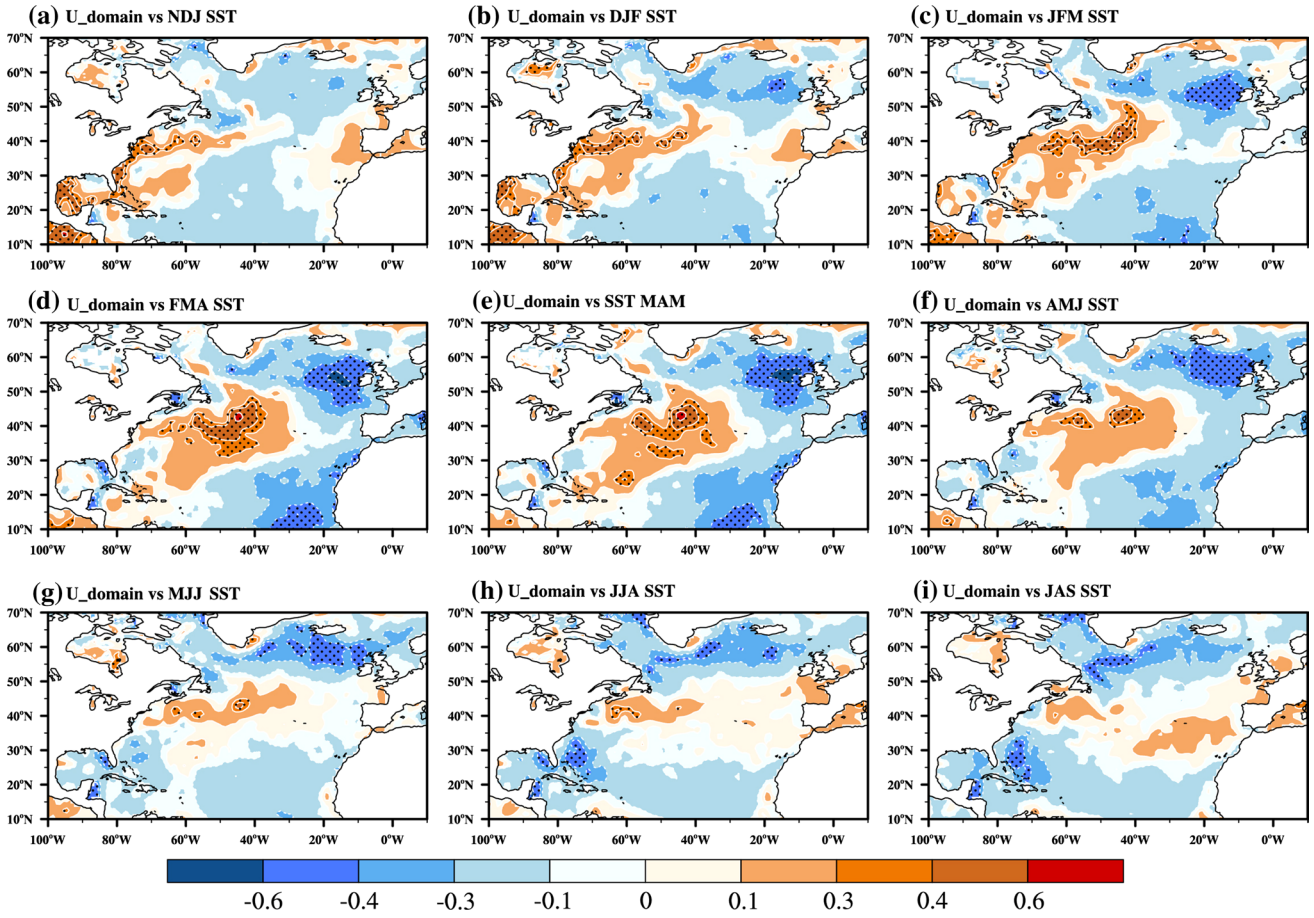

Fig. 2 **a–i** Correlation patterns between the MAM U_domain index and the North Atlantic sea surface temperature (SST) from the preceding November–December–January (NDJ) to July–August–eptember (JAS) during 1980–2008. The SST fields are 1 month sliding between each adjacent panel

these two fields (i.e., heterogeneous correlation fields), respectively. The first SVD mode (SVD1) explains 57 % of the total squared covariance, and the temporal correlation coefficient between the expansion coefficients of SST (SST_SVD1) and that of the 500 hPa zonal wind in SVD1 (U_SVD1) is 0.64, exceeding the 99.9 % confidence level. The 500 hPa zonal wind speed over the TP is characterized by an enhanced WJ over most parts of the TP. Moreover, the SVD1 of zonal wind speed is quite similar to its counterpart of the EOF1 field (Fig. 1a), and the correlation coefficient between U_SVD1 and U_PC1 is 0.91, exceeding the 99.9 % confidence level (Fig. 3d). Also, the SVD1 of SST (Fig. 3b) shows a similar result with its counterpart of the EOF1 (Fig. 3c), characterized by a tripole-like pattern with warm SSTA to the southeast of Newfoundland and cold SSTA to the south of Iceland and southeast of Bermuda. Note that the correlation between the time series of the expansion coefficient of the SST SVD1 and the principal component of SST EOF1 is 0.84, exceeding 99.9 % confidence level (Fig. 3d). All these facts demonstrate that the MAM zonal wind speed at 500 hPa over the TP is closely related to FMA North Atlantic SST in terms of interannual variability.

Based on the results of SVD1 and EOF1 for the North Atlantic SST, we constructed a SST tripole pattern index (SST_tripole hereafter) to discuss the intrinsic connection between the spring zonal wind speed at 500 hPa over the TP and North Atlantic SST. It is defined as the difference between the warm core SSTA in the middle of North Atlantic (the white box in Fig. 3b; 32°–42°N, 60°–40°W) and the sum of two cold cores SSTA in the subtropics (the southern blue box in Fig. 3b; 10°–20°N, 40°:20°W) and subpolar (the northern blue box in Fig. 3b; 50°–60°N, 35°–15°W). The correlation coefficient between SST_tripole index and SST_PC1 (SST_SVD1) is 0.90 (0.94), exceeding 99.9 % confidence level.

We regressed the MAM 500 hPa geopotential height and zonal wind speed against the normalized SST_tripole index, as shown in Fig. 4a, b. In the regressed 500 hPa geopotential height field (Fig. 4a), we can see a four-center

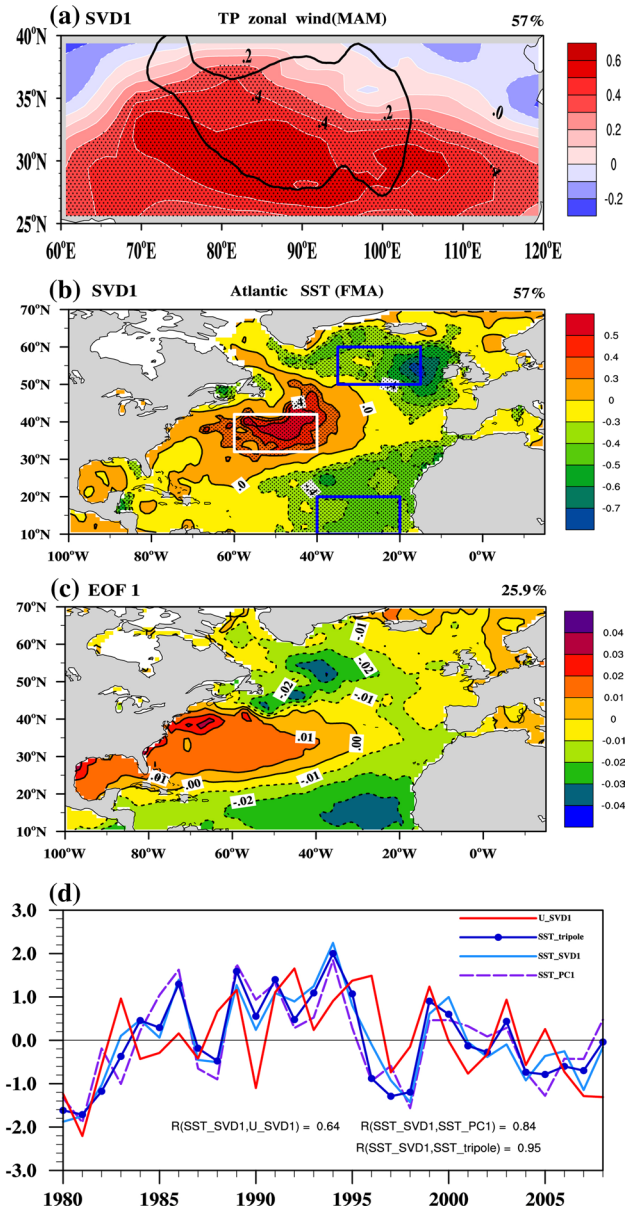

Fig. 3 **a**, **b** Heterogeneous correlation patterns of MAM 500 hPa zonal wind speed over the TP and February–March–April (FMA) SST in the North Atlantic for the first SVD mode during 1980–2008. **c** Spatial pattern of the first EOF mode of the FMA SST in the North Atlantic during 1980–2008; **d** Normalized expansion coefficients of the SVD1 for the FMA North Atlantic SST (SST_SVD1, *cyan line*) and the MAM zonal wind over TP at 500 hPa (U_SVD1, *red line*), the normalized PC1 time series corresponding to the EOF1 of the FMA North Atlantic SST (SST_PC1, *dash purple line*), and the normalized index of the FMA North Atlantic SSTA tripole pattern (SST_tripole, blue marked line). The *heavy solid curves* in **a** and **b** denote the TP domain with altitude higher than 3,000 m above sea level, and the *stippled areas* in (**a**) and (**b**) indicate correlation above the 90 % confidence level. The values in the *top right* corner of (**a**–**c**) are the percentages of explained variance. *White* and *blue boxes* in (**b**) denote one warm and two clod core regions of the SST tripole pattern, respectively. The SST_tripole is defined by the domain-averaged SST in the warm core minus the sum of the domain-averaged SST in the two cold cores

wave train (marked A, B, C and D) extends from the North Atlantic to the northern TP in the mid-level troposphere, exhibiting a south– north-oriented dipole settled over the North Atlantic and a strong positive anomaly located over northern Europe, accompanied by a significant anomalous trough over the northern TP. The dipole anomalies over the North Atlantic are characterized by a positive center along 35°N over the central Atlantic and a negative one over southern Greenland. For convenience, this pattern will be simply referred to as the North Atlantic–Europe–Tibetan Plateau (NAET) wave train throughout the remainder of the paper. Meanwhile, the pattern of MAM zonal wind speed at 500 hPa regressed on FMA SST_tripole index reveals that during the positive SSTA tripole years, the 500 hPa WJ over the TP is significantly stronger than normal (Fig. 4b). The vertical structure of the NAET pattern can be seen in the cross-section of regressed geopotential height along the thick solid lines labeled A, B, C and D in Fig. 4a (Fig. 4c). The NAET pattern has the same phase in the lower, middle and upper troposphere, thereby showing an equivalent barotropic structure in the entire troposphere. The 500-hPa vorticity anomalies can also depict the NAET wave pattern well (Fig. 4d), presenting a stationary wave train crossing the North Atlantic, northern Europe, and the TP. Moreover, diagnosis of the wave activity flux which following Takaya and Nakamura (2001) shows that the wave energy originates above the warm center of the SSTA tripole pattern and propagates eastward until reaching the north of the TP. Therefore, the interannual variability of the subtropical WJ over the TP receives significant impact from the SSTA over the North Atlantic.

According to the time series of FAM SST_tripole index, a composite analysis of MAM geopotential height and temperature was conducted to investigate the differences between strong and weak SSTA tripole pattern years. Two categories were classified by taking the sign of normalized SST_tripole index into account, resulting in six strong positive tripole SSTA years (normalized SST_tripole index >1.0, years: 1986, 1989, 1991, 1993, 1994, 1995) and five strong negative tripole SSTA years (normalized SST_tripole index <−1.0, years: 1980, 1981, 1982, 1997, 1998). During the strong negative tripole SSTA years, the MAM 500-hPa geopotential height is characterized by a trough over the Mediterranean and a ridge over and to the north of the TP (Fig. 5b). However, in strong positive tripole SSTA years, the MAM 500 hPa geopotential height becomes flatter (Fig. 5a), and such a pattern of height contours weakens the heat exchange between the lower and higher latitudes, which is conducive to a larger thermal contrast between the lower and higher latitudes. As a result, the air temperature below 500 hPa is colder over the northern TP but warmer over the southern TP in strong positive FMA tripole SSTA years compared to that in the

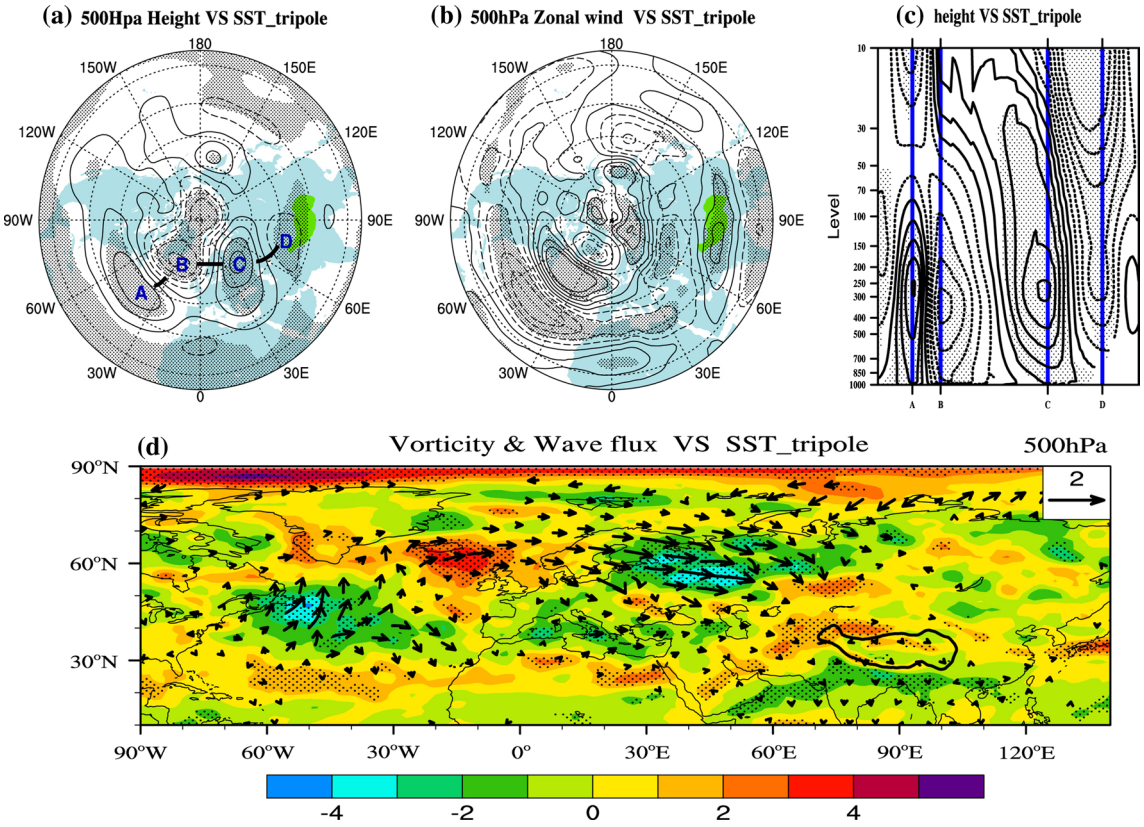

Fig. 4 **a** Regression field of MAM 500 hPa geopotential height against the normalized FMA SST_tripole index from 1980 to 2008 (units: gpm, contour interval is 5gpm and negative contours are *dashed*). **b** The same as (**a**) except for the MAM 500 hPa zonal wind speed (units: m s^{-1}, contour interval is 0.3 m s^{-1} and negative contours are *dashed*). **c** Vertical cross section along the *thick solid lines* labeled *A*, *B*, *C* and *D* in (**a**) for the regression coefficients calculated by MAM geopotential height against FMA SST_tripole index (units: m s^{-1}, contour interval is 5 gpm and negative contours are *dashed*). **d** The same as (**a**) except for MAM Plumb's stationary wave flux at 500 hPa (units: m^2 s^{-2}, *arrows* indicate the correlation above the 90 % confidence level) and MAM 500 hPa vorticity (units: 10^{-6} s^{-1}, *colored shading*). The *stippled areas* in (**a**–**c**) indicate correlation above the 90 % confidence level. The *green shaded areas* in (**a**) and (**b**) and the heavy *solid curve* in (**d**) denote the TP

strong negative tripole SSTA years (shading in Fig. 5c). As required by the thermal wind relationship, the vertical shear of geostrophic wind should be accompanied by a meridional temperature contrast; thus, the increased meridional temperature gradient will enhance the WJ at 500 hPa over the TP during MAM (contours in Fig. 5c).

3.2 The WJ and AHS over the TP

According to Eq. (1), the AHS is composed of three components, i.e., SH, LH and RC. Figure 6a, b are the regression fields of spring SH against the normalized MAM U_domain index during 1980–2008 based on both station data and MERRA reanalysis. During strong WJ years, a positive SH anomaly appears at most stations but especially over the southern TP. Similar results can be seen in the MERRA reanalysis, with a positive anomaly of SH over the southern and northeastern TP but a negative SH anomaly over the northern and central-eastern TP. As Eq. (2) shows, the SH depends mainly on V and ground–air temperature difference ($T_s - T_a$). In order to compare the importances of V and $T_s - T_a$, we regressed both sides of Eq. (2) against U_domain index then divided by $C_p\,\rho\,C_{DH}$

$$\frac{\partial SH/\partial U\_domain}{C_p \rho C_{DH}} = \overline{(T_s - T_a)} \times \partial V/\partial U\_domain + \overline{V} \times \partial (T_s - T_a)/\partial U\_domain \quad (5)$$

Figure 6c, e illustrate the first term (mainly depends on the variation of V) and second term (mainly depends on the variation of $T_s - T_a$) on the right-hand side of Eq. (5) based on station data. The results indicate that the positive SH anomaly corresponds to the positive anomaly of the first term, but the negative SH anomaly corresponds mainly to the negative anomaly of the second term. This means that the enhanced SH mainly results from the increase of the WJ while the reduced SH is mainly caused by the decreased $T_s - T_a$. This result is almost the same in the

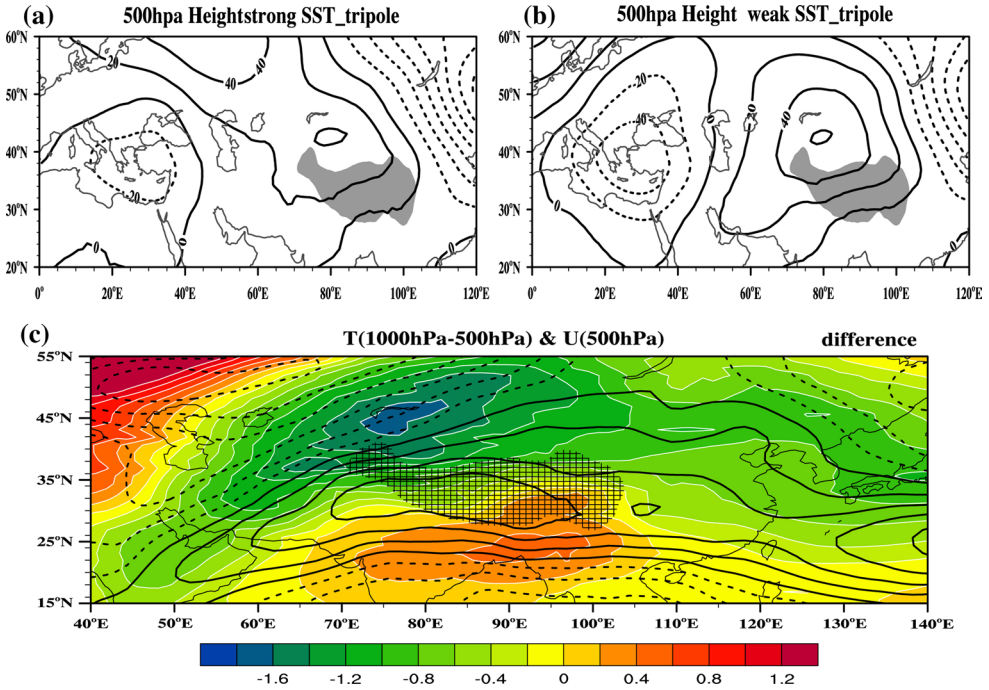

Fig. 5 **a** Composite of the MAM geopotential height at 500 hPa in strong SST anomalous years (years with FMA SST_tripole index greater than 1.0 standard deviation: 1986, 1989, 1991, 1993, 1994,1995) (units: gpm, contour interval is 20 gpm and negative contours are *dashed*). **b** Composite of the MAM geopotential height at 500 hPa in weak SST anomalous years (years with FMA SST_tripole index less than −1.0 standard deviation: 1980, 1981, 1982, 1997, 1998) (units: gpm, contour interval is 20 gpm and negative contours are *dashed*). **c** Difference of the composed MAM mean air temperature from the surface to 500 hPa (units: K, *shading*) and MAM 500 hPa zonal wind speed (units: m s^{-1}, contour interval is 0.5 m s^{-1} and negative contours are *dashed*) between strong SSTA years and weak SSTA years. The zonal mean (from 0°E to 120°E) of geopotential height has been removed in (**a**) and (**b**). *Grey shading* in (**a**) and (**b**) and the *hatched area* in (**c**) represent the TP

MERRA reanalysis (Fig. 6d, f); that is, the positive anomaly of SH over the southern TP is induced mainly by the enhanced WJ, whereas the reduced $T_s - T_a$ is responsible for the negative anomaly of SH over the northern TP. Note that the positive SH anomaly over the southern TP is much larger than the negative SH anomaly over the northern TP, and thus the domain-averaged SH over the TP is obviously above normal in strong WJ years.

The second component of the AHS is LH. The regression field of spring LH against the MAM U_domain index presents a meridional see-saw pattern, with a positive LH anomaly over the northern TP but a negative LH anomaly over the southern TP in both station data (Fig. 7a) and the MERRA reanalysis (Fig. 7b) when the WJ is stronger. The regression fields of the vertically integrated water vapor flux and vertical velocity against U_domain index further demonstrate that, with the intensified WJ over the TP, more moisture will be transported from the tropical oceans to the southwestern and northern TP, and a convergence (divergence) belt of water vapor appears over the northern (southern) TP (Fig. 7c). Since LH is derived directly from precipitation, such a pattern of water vapor flux, in combination with the anomalous ascending motion over the northern TP and abnormal descending motion over the southern TP (Fig. 7d), can explain the north–south seesaw pattern of precipitation and LH over the TP as a response to the anomalous WJ.

The third component of the AHS is RC. As Eq. (4) shows, the net air column radiation flux is composed of four parts, including the net longwave flux and shortwave fluxes at the land surface and TOA, respectively. Figure 8 shows the regression fields of RC and its four components in the MERRA reanalysis against the U_domain index. Although the RC cooling effect is enhanced over most parts of the TP except the southwest fringes and northeastern corner of the TP, the reasons for the RC anomalies over the northern and southern TP are quite different. The negative RC anomaly over the northern TP is induced by the reduction of both net upward longwave flux at the surface and downward shortwave flux at the TOA (Fig. 8b, d). However, the negative RC anomaly over the southern TP is caused by decreased net upward shortwave flux at the surface and increased net upward longwave flux at the TOA (Fig. 8c, e).

Cloud, radiation and precipitation are closely associated. To explore the intrinsic processes among them, we regressed the total cloud amount in both station data and

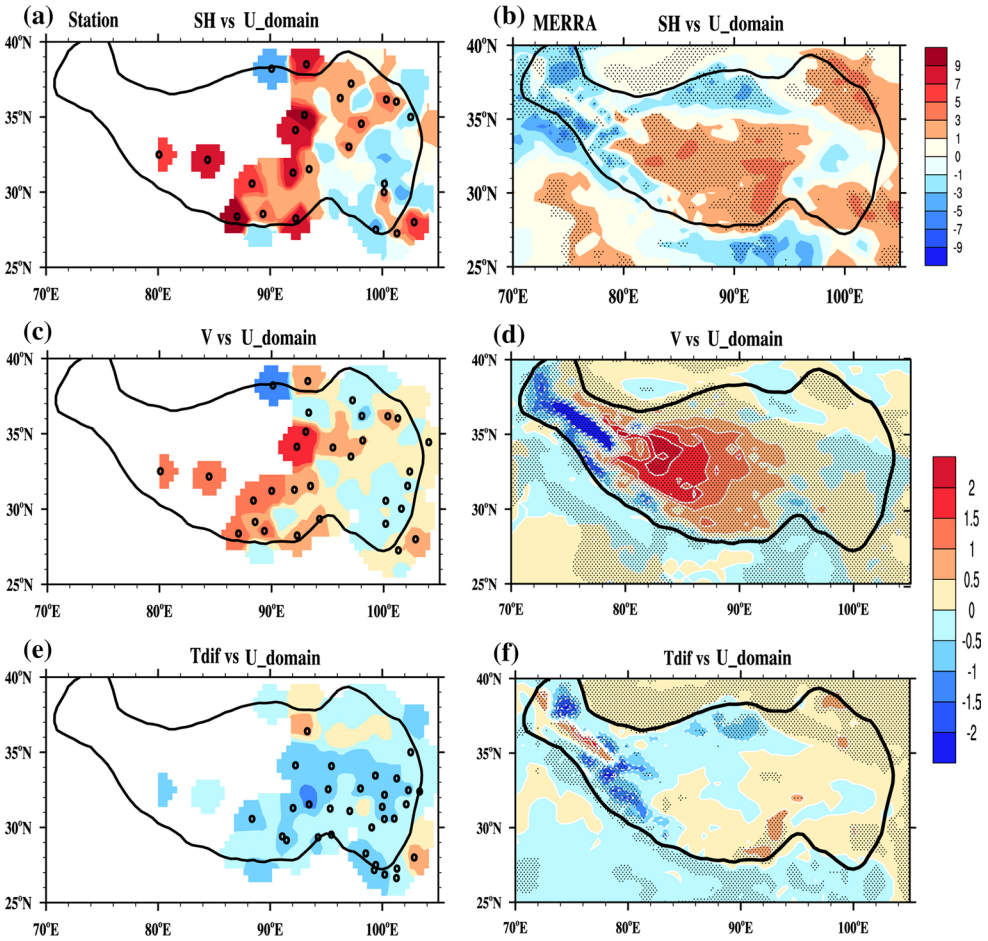

Fig. 6 **a** Regression fields of the MAM surface sensible heating (SH) against the normalized MAM U_domain index during 1980–2008 for station data (units: W m^{-2}). **b** The same as (**a**) except for the SH in the MERRA reanalysis (units: W m^{-2}). **c** Regression fields of the MAM wind speed at 10 m (V) against MAM U_domain index, then multiplied by climatological differences between the MAM ground surface temperature and the MAM 2 m air temperature ($T_s - T_a$) (units: K m s^{-1}) in MAM. **d** The same as (**c**) except for the MERRA reanalysis. **e** Regression fields of $T_s - T_a$ against U_domain index, then multiplied by climate-mean MAM V (units: K m s^{-1}). **f** The same as (**e**) except for the MERRA reanalysis. *Dots* in (**a**, **c**, **e**) and the stippled areas in (**b**, **d**, **f**) indicate correlation above the 90 % confidence level. The *heavy solid curves* in (**a**–**f**) denote the TP

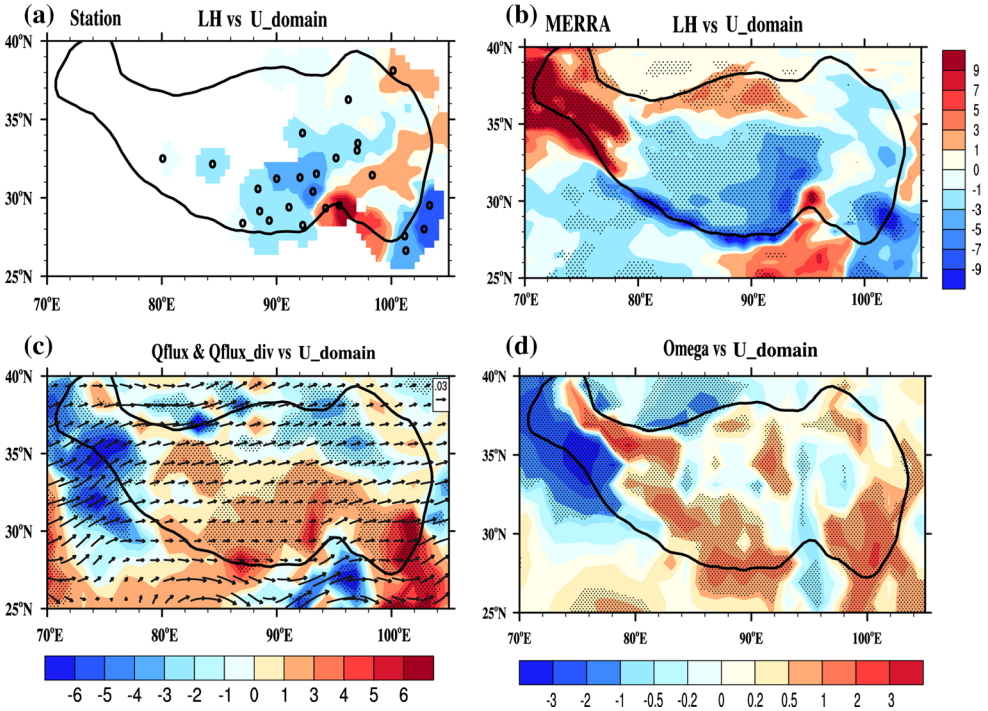

Fig. 7 **a** Regression fields of the MAM latent heating (LH) released to the atmosphere due to condensation against the MAM U_domain index during 1980–2008 for the station data (units: W m^{-2}). **b** The same as (**a**) except for the MAM LH in the MERRA reanalysis. **c** The same as (**b**) except for vertically integrated MAM water vapor flux (units: 100 kg m^{-1} s^{-1}, vectors) and divergence of MAM water vapor flux from the surface to 10 hPa (units: 10^{-6} kg m^{-2} s^{-1}, *shading*). **d** The same as (**a**) except for the MAM vertical pressure velocity, ω (units: 10^{-2} Pa·s^{-1}, dP/dt). *Dots* in (**a**) and the *stippled areas* in (**b**–**d**) indicate correlation above the 90 % confidence level. The *heavy solid curves* in (**a**–**d**) denote the TP

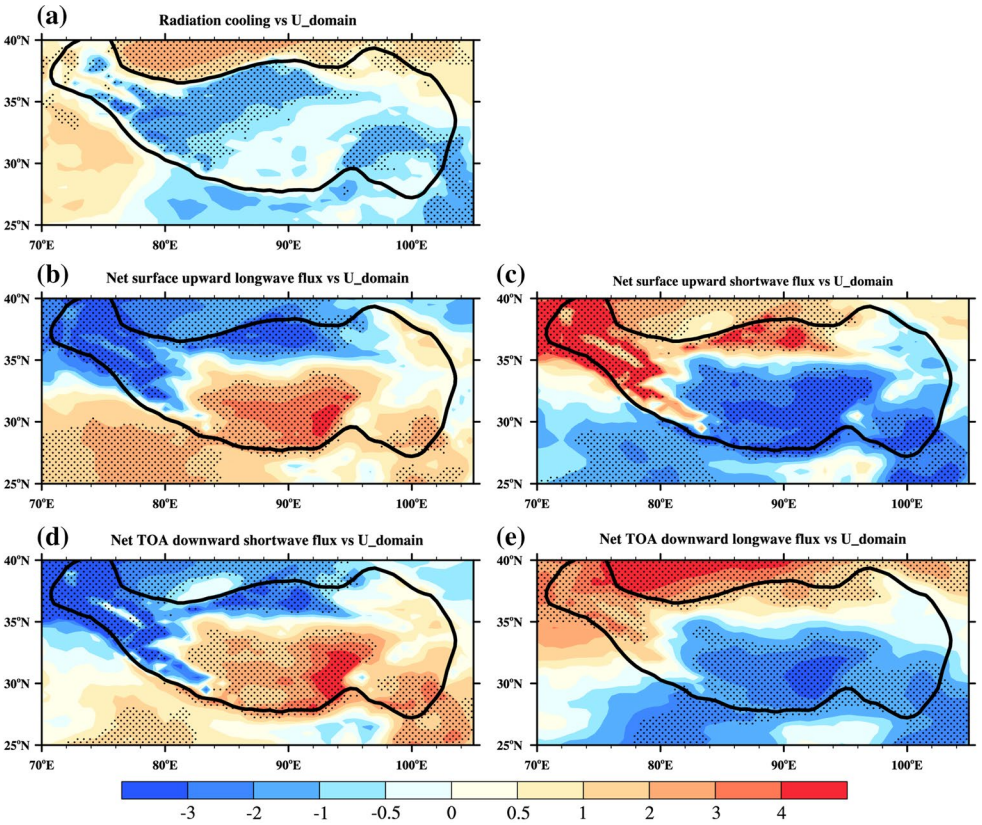

Fig. 8 **a** Regression fields of the MAM air column net radiation flux (RC) calculated from the MERRA reanalysis against the MAM U_domain index during 1980–2008 (units: W m^{-2}). **b** The same as (**a**) except for the MAM net upward longwave flux at the surface (units: W m^{-2}). **c** The same as (**a**) except for the MAM net upward shortwave flux at the surface (units: W m^{-2}). **d** The same as (**a**) except for the MAM net downward shortwave flux at the TOA (units: W m^{-2}). **e** The same as (**a**) except for the MAM net downward longwave flux at the TOA (units: W m^{-2}). The *stippled areas* in (**a**–**e**) indicate correlation above the 90 % confidence level. The *heavy solid curves* in (**a**–**e**) denote the TP

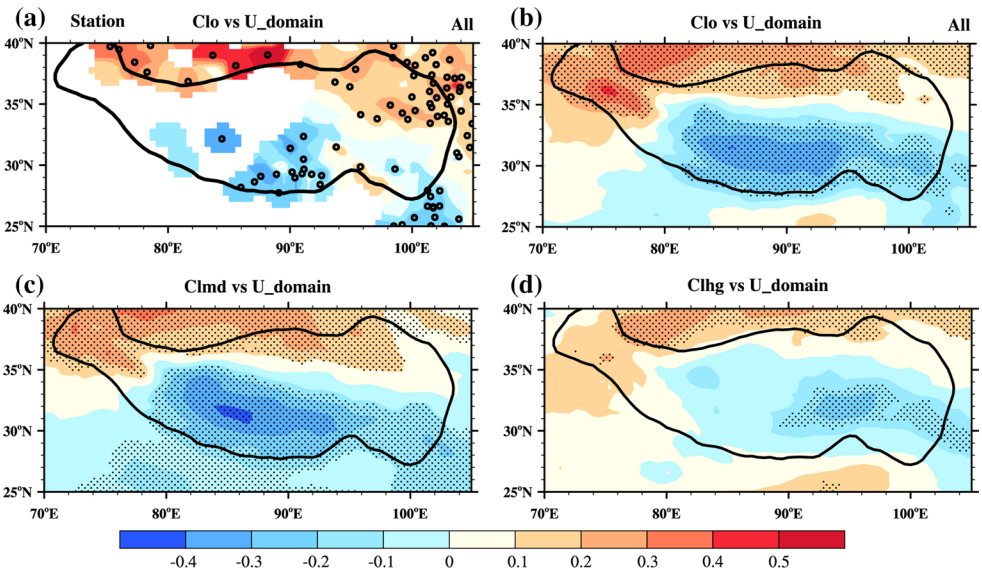

Fig. 9 **a** Regression fields of the MAM total cloud amount (0–10 tenth of sky cover) from the station data over the TP against the MAM U_domain index during 1980–2008. **b** The same as (**a**) except for the MAM total cloud amount in the MERRA reanalysis. **c** The same as (**b**) except for the MAM mid-level cloud amount. **d** The same as (**b**) except for the MAM high-level cloud amount. *Dots* in (**a**) and the *stippled areas* in (**b**–**d**) indicate correlation above the 90 % confidence level. The *heavy solid curves* in (**a**–**d**) denote the TP

the MERRA reanalysis against the U_domain index, as shown in Fig. 9a, b. Despite the coverage limitation of the station data over the TP, the similarity in the basic pattern between station observations and the MERRA reanalysis demonstrates that the total cloud amount will increase (decrease) over the northern (southern) TP when a strong WJ appears. In fact, the north–south seesaw pattern of the total cloud anomaly is contributed to primarily by the mid-level cloud amount (Fig. 9c) rather than the high-level cloud anomaly in the MERRA reanalysis (Fig. 9d). It is important to keep in mind that, due to the very high topography of the TP (the mean surface pressure is close to 600 hPa), the mid-level cloud (700–400 hPa) defined by the MERRA reanalysis over the TP is actually equivalent

to the low-level cloud over low altitude regions. Also, the abnormal convergence (divergence) of water vapor flux over the northern (southern) TP is consistent with a larger (smaller) cloud amount over the northern (southern) TP. During strong WJ years, the precipitation increases over the northern TP can cool down the surface temperature (figure omitted), and the colder land surface further leads to less upward longwave flux, as shown in Fig. 8b. Meanwhile, a larger cloud amount over the northern TP can obstruct solar radiation reaching the atmosphere, so that the downward shortwave flux at the TOA decreases over the northern TP, as shown in Fig. 8d. In contrast, a smaller cloud amount over the southern TP induces more upward longwave radiation flux at the TOA for the blocking effect of cloud on the upward longwave radiation (Fig. 8e), and a smaller low-level cloud amount facilitates more shortwave radiation reaching the ground (Fig. 8c) because low-level cloud can reflect shortwave radiation (Wang et al. 2012b).

As mentioned in some previous studies (e.g., Zhu et al. 2012; Yang et al. 2011), due to the absence of adequate observations for data assimilation and incomplete physical processes in current models, reanalysis datasets show an evident bias over the TP, especially with respect to surface heat fluxes and precipitation. Despite overall similar distributions of SH and LH anomalies between station-based results and the MERRA reanalysis (Figs. 6a, b, 7a, b), the SH anomalies over the TP associated with an above-normal WJ are systematically underestimated in the MERRA reanalysis, whereas the LH anomalies seem to be overestimated compared with the station-based results. Furthermore, by comparing Fig. 8a with Figs. 6b and 7b, we can conclude that the magnitude of RC anomalies is much lower than that of SH and LH anomalies, and hence its contribution to the total AHS might be less important. In spring, the rainy season has not yet started over most parts of the TP, and SH is a major contributor to the AHS over the TP (e.g., Yeh and Gao 1979; Wu et al. 1997; Zhu et al. 2012). Therefore, it is reasonable to speculate that, during strong WJ years, the spring AHS anomalies over the TP are similar to the SH anomalies, and might be above normal. Nevertheless, this hypothesis needs to be verified by more direct observations of diabatic heating over the TP in the future.

4 Numerical simulations

To further elucidate the processes of the anomalous SSTA tripole forcing on the WJ, we performed four numerical experiments with the LBM to simulate the diabatic heating effects of a positive SSTA tripole forcing. The basic state was adopted from the zonally varying early spring (FMA) climatology of the NECP/DOE reanalysis data. The positions of different diabatic forcing sources were determined from the leading mode of the SVD analysis between the North Atlantic SST and 500 hPa zonal wind speed over the TP. The center of the northern diabatic cooling source is located at (55°N, 30°W); the center of the central diabatic heating source is located at (38°N, 57°W), and the center of the southern diabatic cooling source is located at (18°N, 28°W). Each source has an elliptical squared cosine distribution in latitude and longitude with a vertically integrated heating rate of 2.0 K d^{-1} (Fig. 10b), which is comparable-with the diabatic heating anomaly above the warm core in those typical SSTA tripole years (figure not shown here) and previous study on the SSTA tripole pattern over the North Atlantic (Wu et al. 2009). The spatial pattern and vertical heating profile are shown in Fig. 10a, but note that the sign of the vertical profile in the two cooling sources is opposite to the heating source. To compare the importance of each source we prescribed LBM with the northern cooling source in the first experiment, the central heating source in the second experiment, the northern cooling source and central heating source in the third experiment,

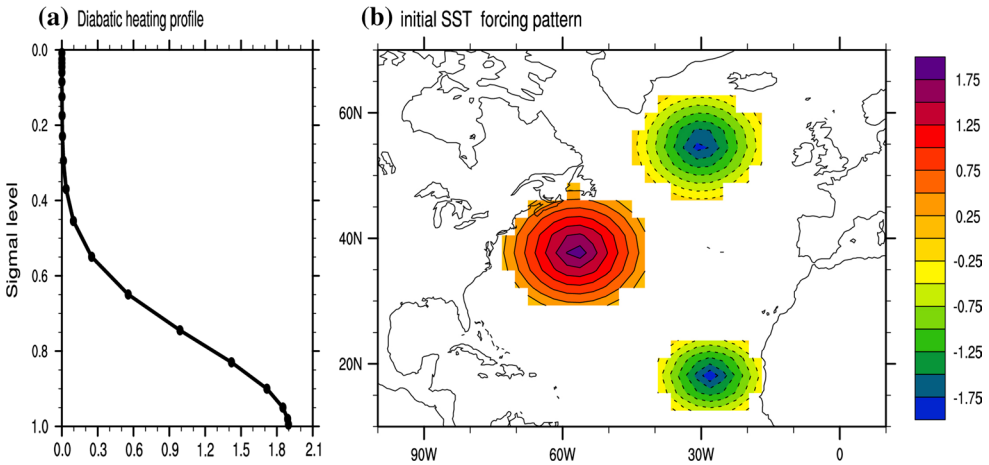

Fig. 10 **a** Specified diabatic heating (units: K d^{-1}) profiles and **b** SST anomaly associated with the positive SSTA tripole pattern over the North Atlantic in the linear baroclinic model (LBM). Note that the sign of the vertical profile is reversed for the two negative SST anomaly centers

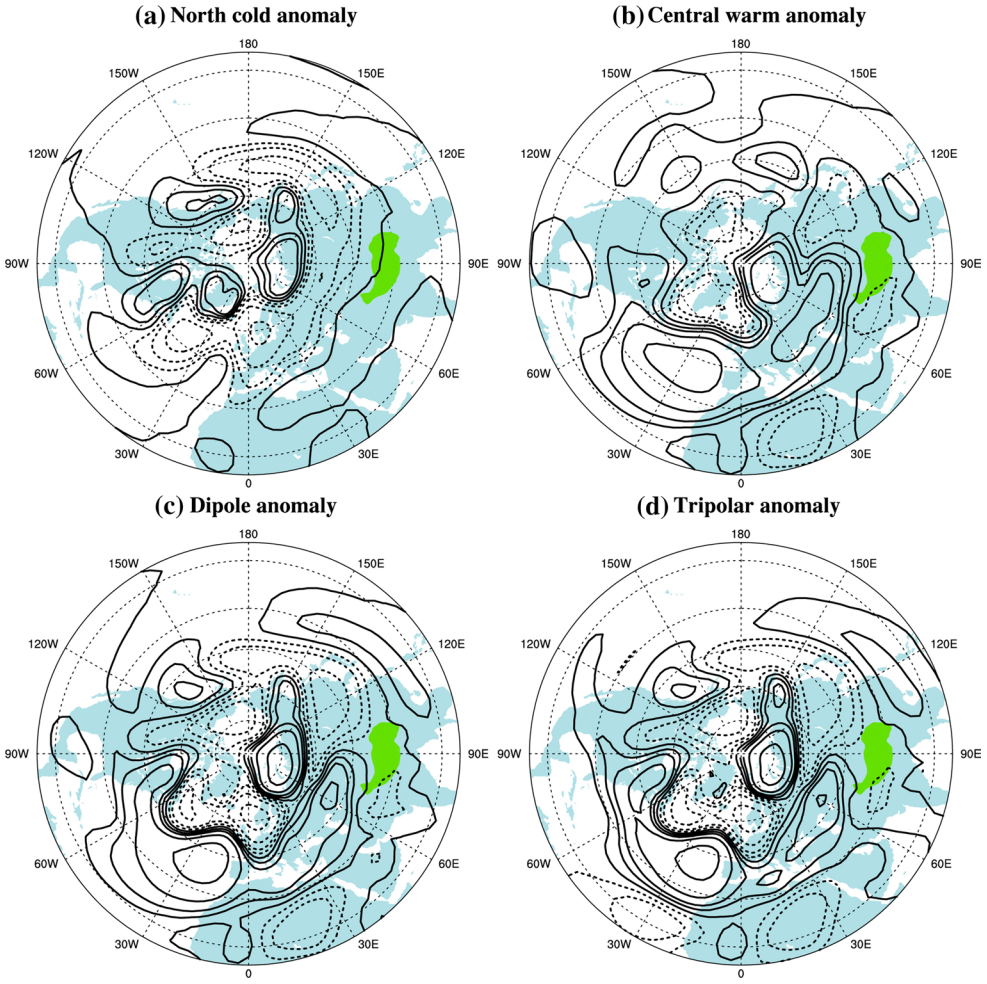

Fig. 11 **a** Response in the 500 hPa geopotential height anomaly (units: gpm, the contours are −16, −8, −4, −2, 0, 2, 4, 8, 16 and negative contours are *dashed*) to the idealized diabatic cooling forcing centered at (55°N, 30°W) in the LBM. **b** The same as (**a**) except for the idealized diabatic heating forcing centered at (38°N, 57°W). **c** The same as (**a**) except for the idealized diabatic cooling forcing centered at (55°N, 30°W) and heating centered at (38°N, 57°W). **d** The same as (**a**) except for the idealized diabatic cooling forcing centered at (55°N, 30°W) and (18°N, 28°W) and heating centered at (38°N, 57°W). The *green shaded* areas in (**a**–**d**) denote the TP

and the complete set of SSTA tripole forcing sources in the fourth experiment.

Figure 11 presents the response of the 500 hPa geopotential height in the four experiments. The results indicate that when only the northern cooling source exists in the North Atlantic, there is no significant wave train in the anomaly field of the 500 hPa geopotential height (Fig. 11a). In contrast, if only the heating source presents (Fig. 11b), a clear 500 hPa wave train similar to the regression field in the MERRA reanalysis (Fig. 4a) appears. Moreover, in the experiments with two forcing sources or the complete set of tripole forcing sources (Fig. 11c, d), the results resemble that in the experiment with only one heating source (Fig. 11b). Therefore, the warm core associated with diabatic heating in the North Atlantic SSTA tripole pattern plays the dominant role in generating and maintaining the spring NAET wave train.

Since there are no feedbacks between diabatic heating (cooling) and circulation in the LBM, and the forcing of the SSTA tripole pattern is represented by the corresponding diabatic heating (cooling) profile instead of the real SSTA in the LBM experiments, we further conducted two sets of ensemble runs based on the SAMIL 2.4.7 AGCM to confirm the results from the LBM model. As mentioned by previous studies (Schneider and Fan 2007; Fan and Schneider 2012; Schneider and Fan 2012), the weather noise cannot be eliminated from the individual model simulation, thus the methodology of extracting the SST-forced response as the ensemble mean of a set of AGCM runs has been employed to remove the influence from weather noise. We designed each set of ensemble included 12 cases integrated from 1 January to 31 May with different initial conditions in the control runs. Differences between the two ensemble means were evaluated. Figure 12a–f presents the composite SSTA fields during strong SSTA years (SST_tripole index greater than 1.0 standard deviation in 1986, 1989, 1991, 1993, 1994, 1995) and weak SSTA years (SST_tripole index less than −1.0 standard deviation in 1980, 1981, 1982, 1997, 1998) from February to April. One set of the AGCM ensemble runs was forced by the climate mean SST during 1990–1999 in Hadley SST from February to April data plus the strong SSTA (Fig. 12a–c) while the SST of rest months remained as the climatology. The other AGCM ensemble runs was forced by the climate mean SST from

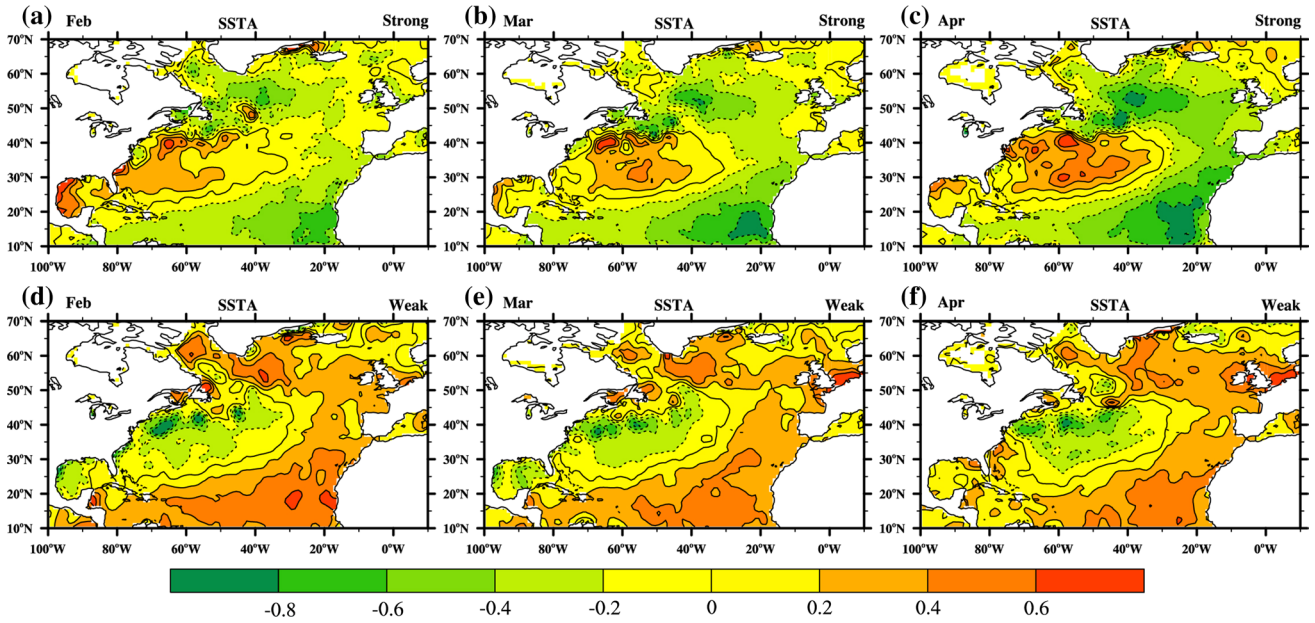

Fig. 12 (**a**–**c**) The anomalous filed of SST over the North Atlantic during the strong SSTA tripole pattern years (SST_tripole index greater than 1.0 standard deviation) from February to April; (**d**–**f**) as (**a**–**c**) but for the anomalous filed of SST during the weak SSTA tripole pattern years (SST_tripole index less than −1.0 standard deviation)

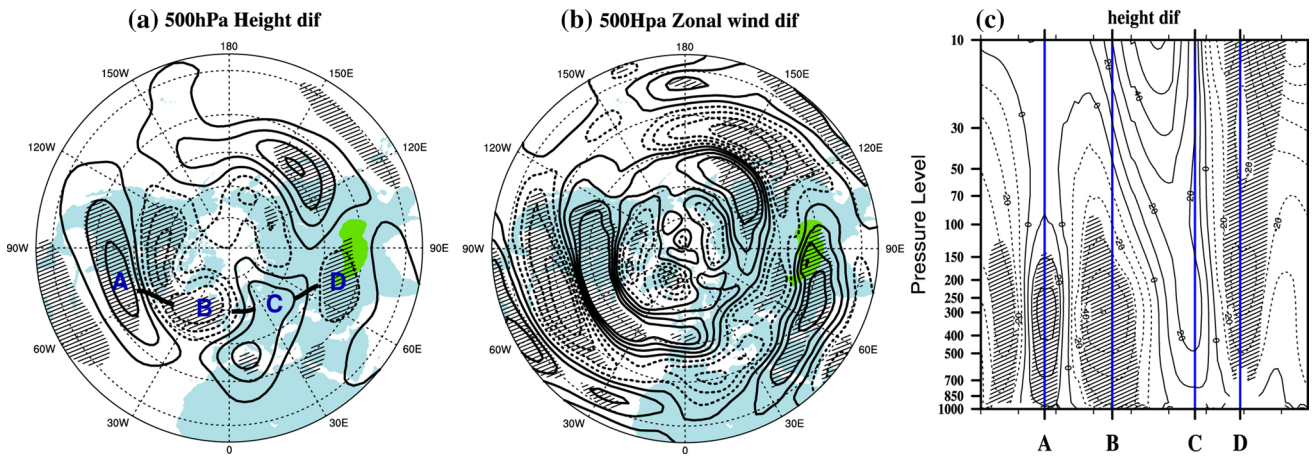

Fig. 13 **a** Difference fields of the MAM 500 hPa geopotential height between positive and negative SSTA cases in the AGCM experiments (units: gpm, contour interval is 8gpm and negative contours are *dashed*). **b** The same as (**a**) except for 500 hPa zonal wind speed (units: m s^{-1} contour interval is 0.6 m s^{-1} and negative contours are *dashed*). (**c**) Vertical cross section along the *thick solid lines* labeled *A*, *B*, *C* and *D* in (**a**) for the composite differences of the MAM geopotential height (units: gpm, contour interval is 10 gpm and negative contours are *dashed*). *Hatched areas* indicate correlation above the 90 % confidence level. The *green shaded* areas in (**a**) and (**b**) denote the TP

February to April plus the weak SSTA (Fig. 12d–f) and the SST of other months remained the climatology.

Figure 13a, b illustrate the difference fields of MAM 500-hPa geopotential height and zonal wind speed between the strong and weak SSTA experiments respectively. The result again shows a wave train similar to that calculated from the MERRA reanalysis, as shown in Fig. 4a, b, especially the positive zonal wind anomaly over the TP. Figure 13c displays the vertical structure of the wave train in the AGCM experiment with SSTA in the North Atlantic, which is characterized by an equivalent barotropic structure in the troposphere, consistent with that derived from the MERRA reanalysis (Fig. 4c). The AGCM simulations further verify the result that the SSTA tripole in the North Atlantic can generate a stationary barotropic Rossby wave to the downstream regions and enhances the WJ over the TP.

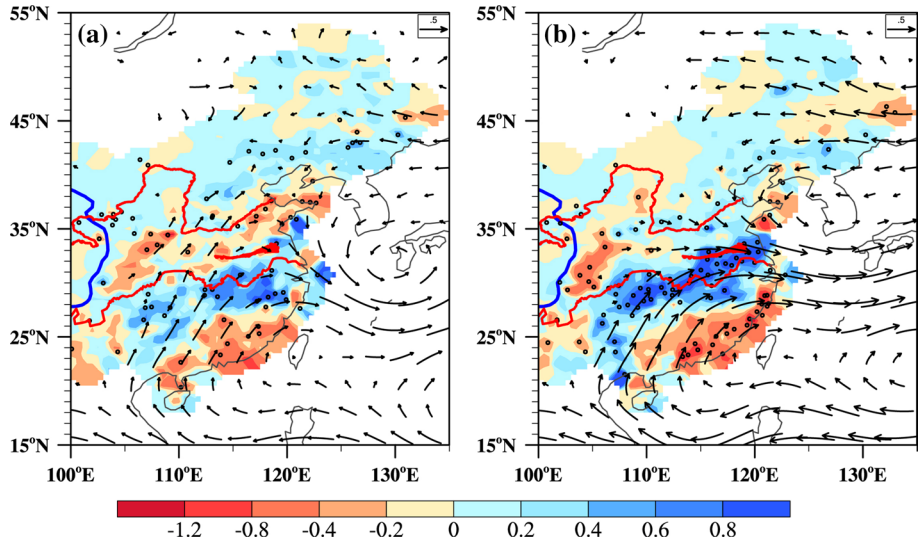

Fig. 14 **a** Regression fields of the summer precipitation (units: mm d^{-1}, *shading*) from the station data and the horizontal wind at 850 hPa (units: m s^{-1}, vectors) against MAM U_domain index during 1980–2008. **b** The same as (**a**) except for summer precipitation (units: mm d^{-1}, *shading*) and summer horizontal wind at 850 hPa (units: m s^{-1}, vectors) against 73-station-averaged MAM SH index over the TP during 1980–2008. *Stippled areas* indicate correlation above the 90 % confidence level. The *red curves* represent the Yangtze, Huaihe and Huanghe rivers from south to north, and the *solid blue curve* denotes the TP

An important fact to note is that, in the AGCM experiments, we could not find a comparable response of the spring AHS over the TP as was found in the station-based results or the MERRA reanalysis. This might be related to model bias in the land surface processes and diabatic heating over the complicated topography (Duan et al. 2014).

5 Seasonal-lagged impact of winter–spring SSTA over the North Atlantic on the EASM

The variability of the NAO is strongest in winter. A previous study suggests that the underlying surface, such as sea ice, SST, and snow cover, provides the memory allowing the winter NAO to affect the summer climate (Ogi et al. 2003). Saunders et al. (2003) argued that enhanced snow cover on the European continent related to the winter NAO can result in cooler summer temperatures over the British Isles and surrounding areas. There are also many studies about the relationship between NAO and EASM. Sung et al. (2006) emphasized the vital role of East Asian westerly jet stream is related to preceding NAO and Yang et al. (2004) pointed the vital role of Middle East jet stream is also related to preceding NAO. However, in these studies the physical mechanism of the preceding NAO influencing subtropical WJ is absent. By conducting a series of AGCM numerical experiments, Duan et al. (2013) found that the enhanced spring SH over the TP can promote the winter-to-summer reversal of land–sea thermal contrast and hence benefits an early onset of the EASM and a strengthening of the EASM circulation system. Moreover, sensitivity experiments using the Weather Research and Forecasting (WRF) model further demonstrate that, through the positive feedback between local atmospheric circulation regimes and diabatic heating, the positive anomaly of spring SH over the TP will facilitate an overall stronger summer AHS over the TP, i.e., the above normal SH (LH) in the western (eastern) TP (Wang et al. 2013). This will further induce excessive summer precipitation along the middle and lower reaches of the Yangtze River and Huaihe River basin. So, is it possible that the SSTA leading mode over the North Atlantic can exert a seasonal-lagged impact upon the EASM by modulating the spring subtropical WJ and AHS over the TP?

Webster and Yang (1992) defined two EASM indexes—one as the vertical shear of meridional wind between 200 hPa and 850 hPa within the area (20°–40°N, 110°–130°E), and another as the vertical shear of zonal wind within (0°–20°N, 60°–100°E). The EASM is known as the typical subtropical monsoon, and some authors have pointed out the meridional wind vertical shear is more significant than zonal wind vertical shear in the EASM region (He et al. 2007; Zhu et al. 2011; Duan et al. 2013). In the present study, we found that the reversal of vertical shear of meridional wind between 200 hPa and 850 hPa will be advanced by about 1 week over the EASM region when the WJ is strong in spring, although the zonal wind vertical shear shows no significant change (figure not shown), suggesting an earlier monsoon onset.

The regression fields of summer precipitation and 850 hPa wind speed against MAM U_domain index

(Fig. 14a) show that a low-level cyclonic anomaly over north China, the Korean peninsula, and Japan brings about a northerly anomaly over north China on its western flank, while an anticyclonic anomaly over the tropical western Pacific means a southwestward extension of the subtropical high and an enhanced low-level southerly on its western flank. Consequently, cold and dry airflow from the mid–high latitudes and warm and wet airflow from tropical oceans converge over the middle and lower reaches of the Yangtze River and Huaihe River basin, accompanied by a positive precipitation anomaly; while the situation over south China is totally different, characterized by a significant negative precipitation anomaly. We also plotted the regression fields of summer precipitation and 850 hPa wind vectors against the spring SH over the TP. The basic spatial pattern of U_domain index related circulation and precipitation anomalies resembles the spring SH index over the TP related pattern, while the positive precipitation anomaly over the middle and lower reaches of the Yangtze River and Huaihe River basin and the negative precipitation anomaly in south China are more significant and well organized. The overall similarity in spatial structure between Fig. 14a, b suggests an important role of the spring SH over the TP in the EASM interannual variability and a close connection between the spring SH and WJ over the TP. However, a few differences between them denote that some other factors, such as local land surface processes, might also influence the SH anomaly to a certain degree. Therefore, we speculate that the late winter to early spring NAO can induce the SSTA tripole pattern in the North Atlantic, which further intensifies the WJ and SH over the TP in spring by exciting a steady Rossby wave train in the downstream regions. As a strong local forcing source, the enhanced spring SH over the TP benefits an early EASM onset and excessive precipitation along the main rainfall belt of the EASM.

6 Conclusions and discussion

Historical records at 73 meteorological stations over the TP, SST from the Hadley Centre, and five reanalysis datasets covering the period 1980–2008 were used to investigate the impacts of the early spring SST tripole pattern over the North Atlantic on the MAM WJ and the AHS over the TP. Numerical sensitivity experiments using an LBM and the SAMIL2.4.7 AGCM were performed to examine the possible mechanisms. The main results of the study can be summarized as follow:

1. The tripole pattern of the early spring SSTA in the North Atlantic, characterized by a positive SSTA to the southeast of Newfoundland and negative SSTA centers to the south of Iceland and southeast of Bermuda, can enhance the MAM WJ over the TP through exciting a stationary barotropic wave train extending from the North Atlantic to the northern part of the TP. The wave train manifests itself as a north–south-oriented dipole settled over the North Atlantic, a strong positive anomaly located over northern Europe, and a significant anomalous trough over the northern TP. It further induces the intensified subtropical WJ over the TP.
2. The spring AHS over the TP is closely related to the WJ at 500 hPa. During strong WJ years, the SH over most of the TP is usually stronger than normal, except for the central-northern TP where the cloud amount and precipitation are enhanced, reducing the land–air temperature difference. Meanwhile, the LH anomaly induced by precipitation shows a seesaw pattern over the TP, characterized by a negative anomaly over the southern TP but a positive anomaly over the northern TP. This is due to the in situ anomalous divergence (convergence) belt of water vapor and descending (ascending) motion over the southern (northern) TP when the WJ is stronger. Although the air column net radiation cooling effect is enhanced over most parts of the TP, the spring AHS over the TP seems to be above normal due to the dominant contribution of SH before the rainy season.
3. The early spring SSTA tripole pattern over the North Atlantic may exert a seasonal-lagged impact upon the EASM by modulating the spring subtropical WJ and SH over the TP. The positive SSTA tripole pattern over the North Atlantic can enhance the spring SH over the TP, which will induce an early EASM onset and excessive precipitation along the main rainfall belt of the EASM.

The mechanism linking the SSTA tripole pattern and EASM provides new information to better understand and predict the EASM. Many previous studies have point out

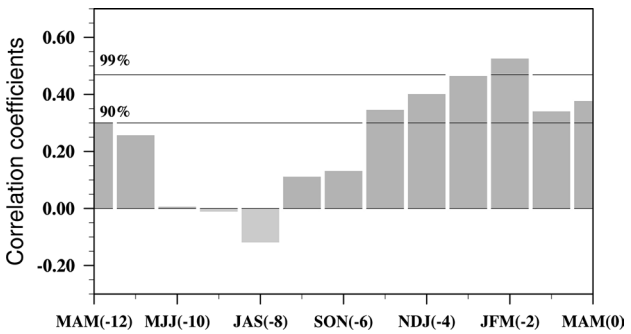

Fig. 15 Lead and lag correlation coefficients between the FAM SST_tripole index and NAO indices. The seasons shown on the abscissa are for the NAO index. The 90 and 99 % significance levels are indicated as *horizontal lines*

the SSTA tripole pattern in the North Atlantic was a result of the NAO (Deser and Timlin 1997). We calculated correlations between the SST_tripole and the 3-month-runing-averaged NAO indices from March to the May (Fig. 15), this FMA SST tripole pattern is correlated to the JFM NAO mostly, the correlation coefficient between JFM NAO index and FMA SST_SVD1 is 0.53 and exceeds 99 % confidence level this implied the preceding NAO is more important than the simultaneous NAO. Herceg-Bulić and Kucharski (2014) has pointed out that the positive winter NAO phase will lead to the North Atlantic SSTA tripole pattern, which can persist from late winter to the following spring due to the long ocean memory. Therefore, we speculate that the JFM NAO stores its influence in the ocean and then affects the MAM zonal wind over the TP by the FMA SSTA in the North Atlantic until boreal spring. From Fig. 15 we can see the correlation coefficients between NAO indexes and FMA SST_tripole declines in JFM and then raise again in MAM, implying a possible positive feedback between NAO and SSTA tripole pattern in the North Atlantic as mentioned by Pan (2005). Some studies have pointed out that the air–sea conditions over the western Pacific can influence the EASM and it might be modulated by the AO/NAO directly or indirectly (Miller et al. 2003; Nakamura et al. 2007; Gong et al. 2009, 2011). Therefore, there might be two possible ways in which the winter–spring NAO and associated SSTA pattern over the North Atlantic affect the EASM. One is by modulating the land surface conditions over the continent, such as the influence from the anomalous SH over the TP as discussed in this work. The other is by modulating the air–sea conditions over the western Pacific and tropical Pacific. It is important to separate these two influences and their possible interaction. In future, numerical experiments with air–sea coupled climate models are needed to distinguish the influence from the SSTA over the western Pacific with that from SH over the TP.

Acknowledgments This work was supported jointly by the National Natural Science Foundation of China (Grant Nos. 91337216, 41175070 and 40925015) and the Special Fund for Public Welfare Industry (meteorology) administered by the Chinese Ministry of Finance and Ministry of Science and Technology (Grant No. GYHY201406001).

References

Bretherton CS, Smith C, Wallace JM (1992) An intercomparison of methods for finding coupled patterns in climate data. J Clim 5:541–560

Cayan DR (1992a) Latent and sensible heat flux anomalies over the Northern Oceans: the connection to monthly atmospheric circulation. J Clim 5:354–369

Cayan DR (1992b) Latent and sensible heat flux anomalies over the northern oceans: driving the sea surface temperature. J Phys Oceanogr 22:859–881

Chen LX, Reiter E, Feng ZQ (1985) The atmospheric heat source over the Tibetan Plateau: May–August 1979. Mon Weather Rev 113:1771–1790

Czaja A, Frankignoul C (2002) Observed impact of Atlantic SST anomalies on the North Atlantic Oscillation. J Clim 15:606–623

Dai FS, Yu RC, Zhang XH, Yu YQ (2004) A statistical low-level cloud scheme and its tentative application in a general circulation model (in Chinese). Acta Meteorol Sin 62:385–394

Dee DP, Uppala SM, Simmons AJ, Berrisford P, Poli P, Kobayashi S, Andrae U, Balmaseda A, Balsamo G, Bauer P, Bechtold P, Beljaars ACM, van de Berg L, Bidlot J, Bormann N, Delsol C, Dragani R, Fuentes M, Geer AJ, Hamiberger L, Healy SB, Hersbach H, Holm EV, Isaksen L, Kallberg P, Köhler M, Matricardi M, Mcnally AP, Monge-sanz BM, Morcrette JJ, Park BK, Peubey C, De Rosnay P, Tavolato C, Thepaut JN, Vitart F (2011) The ERA-Interim reanalysis: configuration and performance of the data assimilation system. Q J R Meteorol Soc 137:553–597

Deser C, Timlin M (1997) Atmosphere-ocean interaction on weekly timescales in the North Atlantic and Pacific. J Clim 10:393–408

Duan A, Wu G (2009) Weakening trend in the atmospheric heat source over the Tibetan Plateau during recent decades. Part II: connection with climate warming. J Clim 22:4197–4212

Duan A, Wang MR, Lei YH, Cui YF (2013) Trends in summer rainfall over China associated with the Tibetan Plateau sensible heat source during 1980–2008. J Clim 25:261–274. doi:10.1175/JCLI-D-11-00669.1

Duan A, Xiao ZX, Hu J (2014) Can current AGCMs reproduce historical changes in the atmospheric diabatic heating over the Tibetan Plateau? Atmos Ocean Sci Lett 7:143–148

Edwards JM, Slingo A (1996) Studies with a flexible new radiation code. I: choosing a configuration for a large-scale model. Q J R Meteorol Soc 122:689–719

Fan M, Schneider EK (2012) Observed decadal North Atlantic tripole SST variability. Part I: weather noise forcing and coupled response. J Atmos Sci 69(1):35–50

Flohn H (1957) Large-scale aspects of the summer monsoon in South and East Asia. J Meteorol Soc Jpn 35:180–186

Gong DY, Ho CH (2003) Arctic oscillation signals in the East Asian summer monsoon. J Geophys Res 108:4066. doi:10.1029/2002JD002193

Gong DY, Kim SJ, Ho CH (2009) Arctic and Antarctic Oscillation signature in tropical coral proxies over the South China sea. Ann Geophys 27:1979–1988

Gong DY, Yang J, Kim SJ, Gao Y, Guo D, Zhou T, Hu M (2011) Spring Arctic Oscillation-East Asian summer monsoon connection through circulation changes over the western North Pacific. Clim Dyn 37:2199–2216

He JH, Qi L, Wei J, Chi YZ (2007) Reinvestigations on the East Asian subtropical monsoon and tropical monsoon. Chin J Atmos Sci 31(6):1257

Herceg-Bulić I, Kucharski F (2014) North Atlantic SSTs as a link between the Wintertime NAO and the following spring climate. J Clim 27:186–201

Holtslag AAM, Boville BA (1993) Local versus nonlocal boundary-layer diffusion in a global climate model. J Clim 6:1825–1842

Kalnay E, Kanamitsu M, Kistler R, Collins W, Deaven D, Gandin L, Iredell M, Saha S, White G, Woollen J, Zhu Y, Leetmaa A, Reynolds R, Chelliah M, Ebisuzaki W, Higgins W, Janowiak J, Mo KC, Ropelewski C, Wang J, Jenne R, Joseph D (1996) The NCEP/NCAR 40-year reanalysis project. Bull Am Meteorol Soc 77:437–471

Kanamitsu M, Ebisuzaki W, Woollen J, Yang SK, Hnilo JJ, Fiorino M, Potter GL (2002) NCEP–DOE AMIP-II Reanalysis (R-2). Bull Am Meteorol Soc 83:1631–1643

Li CF, Yanai M (1996) The onset and interannual variability of the Asian summer monsoon in relation to land-sea thermal contrast. J Clim 9:358–375

Li GP, Duan TY, Gong YF (2000) The bulk transfer coefficients and surface fluxes on the western Tibetan Plateau (in Chinese). Chin Sci Bull 45:865–869

Li GP, Duan TY, Haginoya S, Chen LX (2001) Estimates of the bulk transfer coefficients and surface fluxes over the Tibetan using AWS data. J Meteorol Soc Jpn Ser 2 79(2):625–635

Li J, Yu R, Zhou T, Wang B (2005) Why is there an early spring cooling shift downstream of the Tibetan Plateau? J Clim 18:4660–4668

Li J, Yu R, Zhou T (2008) Teleconnection between NAO and Climate Downstream of the Tibetan Plateau. J Clim 21:4680–4690

Liu G, Zhao P, Wu R, Chen J (2012) Potential flaws of interdecadal changes over eastern China around the early 1990s in the National Centers for Environmental Prediction– National Center for Atmospheric Research reanalyses. J Geophys Res 117:D02111. doi:10.1029/2011JD016327

Marshall J, Kushnir Y, Battisti D, Chang P, Czaja A, Dickson R, Hurrell J, McCartney M, Saravanan R, Visbeck M (2001) North Atlantic climate variability: phenomena, impacts and mechanisms. Int J Climatol 21:1863–1898. doi:10.1002/joc.693

Miller AJ, Zhou S, Yang SK (2003) Relationship of the Arctic and Antarctic Oscillations to the outgoing longwave radiation. J Clim 16:1583–1592

Murakami T, Ding YH (1982) Wind and temperature changes over Eurasia during the early summer of 1979. J Meteorol Soc Jpn 60:183–196

Nakamura T, Tachibana Y, Shimoda H (2007) Importance of cold and dry surge in substantiating the NAM and ENSO relationship. Geophys Res Lett 34:L22703. doi:10.1029/2007GL031220

Nordeng TE (1994) Extended versions of the convective parameterization scheme at ECMWF and their impact on the mean and transient activity of the model in the tropics. ECMWF Technical Memorandum 206

Ogi M, Tachibana Y, Yamazaki K (2003) Impact of the wintertime North Atlantic Oscillation (NAO) on the summertime atmospheric circulation. Geophys Res Lett 30(13):1704. doi:10.1029/2003GL017280

Onogi K, Tsutsui J, Koide H, Sakamoto M, Kobayashi S, Hatsushika H, Matsumoto T, Yamazaki N, Kamahori H, Takahashi K, Kadokura S, Wada K, Kato K, Oyama R, Ose T, Mannoji N, Taira R (2007) The JRA-25 Reanalysis. J Meteorol Soc Jpn 85:369–432

Palmer TN, Shutts GJ, Swinbank R (1986) Alleviation of a systematic westerly bias in general circulation and numerical weather prediction models through an orographic gravity wave drag parameterization. Q J R Meteorol Soc 112:1011–1039

Pan L (2005) Observed positive feedback between the NAO and the North Atlantic SSTA tripole. Geophys Res Lett 32:L06707. doi:10.1029/2005GL022427

Rayner NA, Parker DE, Horton EB, Folland CK, Alexander LV, Rowell DP, Kent EC, Kaplan A (2003) Global analyses of sea surface temperature, sea ice, and night marine air temperature since the late nineteenth century. J Geophys Res Atmos (1984–2012). 108:4407. doi:10.1029/2002JD002670

Rienecker MM, Suarez MJ, Gelaro R, Todling R, Bacmeister J, Liu E, Bosilovich MG, Schubert SD, Takacs L, Kim GK, Bloom S, Chen J, Collins D, Conaty A, da Silva A, Gu W, Joiner J, Koster RD, Lucchesi R, Molod A, Owens T, Pawson S, Pegion P, Redder CR, Reichle R, Robertson FR, Ruddick AG, Sienkiewicz M, Woollen J (2011) MERRA: NASA's Modern-Era retrospective analysis for research and applications. J Clim 24:3624–3648. doi:10.1175/JCLI-D-11-00015.1

Saunders MA, Qian B, Lloyd-Hughes B (2003) Summer snow extent heralding of the winter North Atlantic Oscillation. Geophys Res Lett 30:7

Schneider EK, Fan M (2007) Weather noise forcing of surface climate variability. J Atmos Sci 69:51–64

Schneider EK, Fan M (2012) Observed decadal North Atlantic tripole SST variability. Part II: diagnosis of mechanisms. J Atmos Sci 69:51–64

Shen RJ, Reiter ER, Bresch JF (1986) Some aspects of the effects of sensible heating on the development of summer weather systems over the Tibetan Plateau. J Atmos Sci 43:2241–2260

Slingo JM (1980) A cloud parameterization scheme derived from GATE data for use with a numerical model. Q J R Meteorol Soc 106:747–770

Slingo JM (1989) A GCM parameterization for the shortwave radiative properties of water clouds. J Atmos Sci 46:1419–1427

Song XL (2005) The evaluation analysis of two kinds of mass flux cumulus parameterizations in climate simulation (in Chinese). Ph.D. dissertation, Institute of Atmospheric Physics, Chinese Academy of Sciences

Sun ZA (2005) Parameterizations of radiation and cloud optical properties. BMRC research report

Sung MK, Kwon WT, Baek HJ, Boo KO, Lim GH, Kug JS (2006) A possible impact of the North Atlantic Oscillation on the east Asian summer monsoon precipitation. Geophys Res Lett 33(21):21713

Takaya K, Nakamura H (2001) A formulation of a phase-independent wave-activity flux for stationary and migratory quasigeostrophic eddies on a zonally varying basic flow. J Atmos Sci 58:608–627

Tiedtke M (1989) A comprehensive mass flux scheme for cumulus parameterization in large-scale models. Mon Weather Rev 117:1779–1800

Wang J, Bao Q, Liu YM, Wu GX, He B, Wang XC (2012a) Performances of SAMIL on the global heating and the East Asian summer monsoon (in Chinese). Chin J Atmos Sci 36:63–76

Wang X, Liu Y, Bao Q, Wang Z (2012b) Climate sensitivity and cloud feedback processes imposed by two different external forcing in an aquaplanet GCM. Theoret Appl Climatol 110:1–10

Wang ZQ, Duan A, Wu GX (2013) Time-lagged impact of spring sensible heat over the Tibetan Plateau on the summer rainfall anomaly in East China: case studies using the WRF model. Clim Dyn 1:244

Watanabe M, Jin FF (2003) A moist linear baroclinic model: coupled dynamical–convective response to El Nin ˜o. J Clim 16:1121–1139

Watanabe M, Kimoto M (2000) Atmosphere ocean thermal coupling in the North Atlantic: a positive feedback. Q J R Meteorol Soc 126:3343–3369

Watanabe M, Kimoto M, Nitta T (1999) A comparison of decadal climate oscillations in the North Atlantic detected in observations and a coupled GCM. J Clim 12:2920–2940. doi:10.1175/1520-0442(1999)012<2920:ACODCO>2.0.CO;2

Webster PJ, Yang S (1992) Monsoon and ENSO: selectively interactive systems. Q J R Meteorol Soc 118:877–926

Wu G, Liu H, Zhao Y, Li W (1996) A nine-layer atmospheric general circulation model and its performance. Adv Atmos Sci 13:1–18

Wu GX, Li W, Guo H, Liu H, Xue J, Wang Z (1997) Sensible heat driven air-pump over the Tibetan Plateau and its impacts on the Asian summer monsoon. Collections on the memory of Zhao Jiuzhang. Chinese Science Press, Beijing, pp 116–126

Wu GX, Liu Y, Wang T, Wan R, Liu X, Li W, Liang X (2007) The influence of mechanical and thermal forcing by the Tibetan Plateau on Asian climate. J Hydrometeorol 8(4):770–789

Wu Z, Wang B, Li J, Jin FF (2009) An empirical seasonal prediction model of the east Asian summer monsoon using ENSO and NAO. J Geophys Res 114:D18120. doi:10.1029/2009JD011733

Wu GX, Liu YM, He B, Bao Q, Duan AM, Jin FF (2012) Thermal controls on the Asian summer monsoon. Sci Rep 2:404. doi:10.1038/srep00404

Yanai M, Li C (1994) Mechanism of heating and the boundary layer over the Tibetan Plateau. Mon Weather Rev 122:305–323

Yang S, Lau K-M, Yoo S-H, Kinter JL, Miyakoda K, Ho C-H (2004) Upstream subtropical signals preceding the Asian summer monsoon circulation. J Clim 17:4213–4229

Yang K, Guo X, He J, Qin J, Koike T (2011) On the Climatology and trend of the Atmospheric Heat Source over the Tibetan Plateau: an experiments-supported revisit. J Clim 24(5):1525–1541

Yeh TC, Gao YX (1979) Meteorology of the Qinghai-Xizang (Tibet) Plateau. Science Press, Beijing (in Chinese)

Yeh TC, Lo SW, Chu PC (1957) On the heat balance and circulation structure in troposphere over Tibetan Plateau (in Chinese). Acta Metorol Sinica 28:108–121

Yu JJ, Liu YM, Wu GX (2011a) An analysis of the diabatic heating characteristic of atmosphere over the Tibetan Plateau in winter I: climatology. Acta Meteorologica Sinica 69:79–88

Yu JJ, Liu YM, Wu GX (2011b) An analysis of the diabatic heating characteristic of atmosphere over the Tibetan Plateau in winter II: interannal variation. Acta Meteorologica Sinica 69:89–98

Zhao P, Chen LX (2001) Climatic features of atmospheric heat source/sink over the Qinghai-Xizang Plateau in 35 years and its relation to rainfall in China. Sci China Ser D 44:858–864

Zhou T, Yu R, Gao Y, Drange H (2006) Ocean- atmosphere coupled model simulation of North Atlantic interannual variability I: local air–sea interaction. Acta Meteorologica Sinica 64:1–17 (in Chinese)

Zhu CW, Zhou XQ, Zhao P, Chen LX, He JH (2011) Onset of East Asian Sub-tropical Summer Monsoon and Rainy Season in China Earth. Sci China Earth Sci. doi:10.1007/s11430-011-4284-0

Zhu XY, Liu YM, Wu GX (2012) An assessment of summer sensible heat flux on the Tibetan Plateau from eight data sets. Sci China Earth Sci 55:779–786. doi:10.1007/s11430-012-4379-2